J. Fluid Mech. (1979), *vol.* 95, *part* 3, *pp.* 477–495
Printed in Great Britain

Natural convection in thermally stratified enclosures with localized heating from below

By K. E. TORRANCE

Sibley School of Mechanical and Aerospace Engineering,
Cornell University, Ithaca, New York 14853

(Received 6 August 1976 and in revised form 2 April 1979)

Natural convection flows induced by localized heating of the base of a thermally stratified enclosure are examined. The enclosure is a vertical circular cylinder with height equal to radius. The wall temperature increases linearly with height, and a small heat source is centrally located on the floor. Parameters of the problem are the ambient stratification rate (Γ^{-1}), the Prandtl number (Pr), and a Grashof number (Gr) based on the temperature and the diameter of the heated spot. Over wide ranges of Γ and Gr, vertically layered convection cells are observed in the upper part of the enclosure in both laboratory experiments and numerical calculations. For the case of strong buoyancy and weak stratification, plume-like flows exist immediately above the heat source. Streak photographs are in qualitative accord with the numerical calculations, except for a range of Gr when an azimuthal rotation of the laboratory plume is observed. All flows are otherwise laminar. The theoretical results reveal a $\sqrt{Gr}$ scaling at large Gr for the velocities and heat transfer rates, and a correlation of strongly stratified, viscous flows with the group $Gr\,Pr\,\Gamma^{-1}$.

1. Introduction

Natural convection flows are strongly influenced by the presence of a gravitationally stable, ambient density gradient. Indeed, results for external flows such as plumes and boundary layers have been summarized by Turner (1973). On the other hand, results for internal, cavity flows with stratification are somewhat less extensive, but include the studies of Walin (1971) and Chen, Briggs & Wirtz (1971). A unique feature of the latter study was the observation of vertically layered convection cells when the lateral boundaries were differentially heated. The present study considers fluid motion in a thermally stratified enclosure when the motion is induced by localized heating at the lower boundary. A specific objective of the study is to determine whether plume flows or layered convection cells exist, and the relative importance of the two modes of convection.

Prior studies have examined enclosure flows driven by localized heating from below, but without ambient stratification (Torrance & Rockett 1969; Knight 1976; and others). A prior study by Delage & Taylor (1970) has considered the flow induced in a stably stratified, horizontally unbounded fluid region (the atmosphere) by localized bottom heating (a city). Numerical solutions were reported for a two-dimensional Cartesian geometry. Corresponding results for enclosures, or for axisymmetric geometries, are not available. The present paper considers the recirculating flows induced in an axisymmetric, thermally stratified, cylindrical enclosure by a heat source

0022-1120/79/4331-7740 $02.00

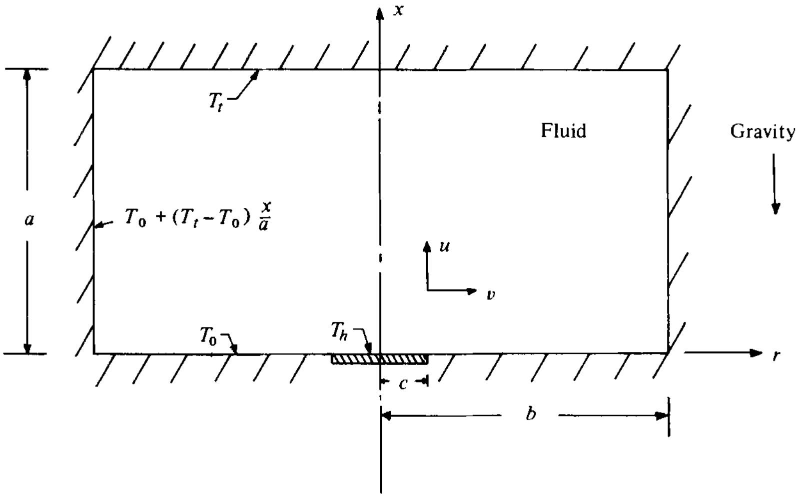

FIGURE 1. Cylindrical enclosure and co-ordinate system.

located in the centre of the base. Both experimental and numerical solutions are reported. Results are presented in terms of streamline and temperature fields. The effects of ambient stratification, heat-source strength, and Prandtl number are investigated. Also considered in detail are representative velocity profiles and heat transfer characteristics.

2. Problem formulation

Consider the vertical cylindrical enclosure of height a and radius b illustrated in figure 1. An x, r co-ordinate system is located in the centre of the base. The top is maintained at a temperature T_t which is higher than the temperature T_0 of the base, i.e. $T_t \geqslant T_0$. The temperature of the vertical wall varies linearly from floor to ceiling. In the base, a small, centrally located disk of radius c is maintained at a temperature T_h which is higher than the temperature T_0 of the surrounding floor. Characteristic temperature differences thus emerge for the horizontal and vertical directions:

$$\Delta T_H \equiv T_h - T_0, \quad \Delta T_V \equiv T_t - T_0. \tag{1}$$

The horizontal temperature difference ΔT_H serves to induce and sustain a natural convection flow in the enclosure. The vertical temperature difference ΔT_V influences and controls the vertical structure of the induced flow.

Using ΔT_H as reference temperature, heat-source diameter $(2c)$ as reference length, and the ratio $(2c)^2/\kappa$ as reference time (κ = fluid thermal diffusivity), the governing equations in dimensionless form become:

$$u = \frac{1}{r}\frac{\partial \psi}{\partial r}, \quad v = -\frac{1}{r}\frac{\partial \psi}{\partial x}, \tag{2}$$

$$\frac{1}{r}\frac{\partial^2 \psi}{\partial x^2} + \frac{\partial}{\partial r}\left(\frac{1}{r}\frac{\partial \psi}{\partial r}\right) = -\omega, \tag{3}$$

$$\frac{\partial \omega}{\partial t}+\frac{\partial(u\omega)}{\partial x}+\frac{\partial(v\omega)}{\partial r} = -Gr\,Pr^2\frac{\partial \theta}{\partial r}+Pr\left\{\frac{\partial^2\omega}{\partial x^2}+\frac{\partial}{\partial r}\left(\frac{1}{r}\frac{\partial r\omega}{\partial r}\right)\right\}, \tag{4}$$

$$\frac{\partial \theta}{\partial t}+\frac{\partial(u\theta)}{\partial x}+\frac{1}{r}\frac{\partial(rv\theta)}{\partial r}+\frac{1}{A\Gamma}u = \frac{\partial^2\theta}{\partial x^2}+\frac{1}{r}\frac{\partial}{\partial r}\left(r\frac{\partial \theta}{\partial r}\right). \tag{5}$$

Axisymmetric motion and the Boussinesq approximation are assumed. The variables are the axial and radial velocity components u and v, stream function ψ, azimuthal vorticity ω, and a dimensionless temperature defined relative to the wall temperature at the same height

$$\theta \equiv [T(x,r)-T(x,b)]/\Delta T_H.$$

Since θ is defined relative to the ambient temperature gradient (assumed constant), a term $u/A\Gamma$ appears in (5). This term, with coefficients to be defined subsequently, describes vertical convection of the ambient stratification gradient.

The governing equations introduce three dimensionless parameters: a Grashof number, a Prandtl number, and a stratification ratio, defined by

$$Gr = g\beta\Delta T_H(2c)^3/\nu^2, \quad Pr = \nu/\kappa, \quad \Gamma = \Delta T_H/\Delta T_V, \tag{6}$$

where ν denotes the kinematic viscosity, β the volume thermal expansion coefficient, and g the acceleration of gravity. The stratification parameter Γ denotes the ratio of horizontal and vertical temperature differences. This particular choice facilitates comparison with the laboratory experiments. The case $\Gamma = 0$ corresponds to a quiescent thermally stratified enclosure, whereas $\Gamma = \infty$ corresponds to natural convection above the heated disk without ambient stratification.

The enclosure geometry introduces two dimensionless parameters: the height and radius of the enclosure, given by

$$A = a/2c \quad \text{and} \quad B = b/2c. \tag{7}$$

Thus, the product $A\Gamma$ appearing in (5) represents the inverse of a dimensionless ambient temperature gradient.

Initial conditions are arbitrary and are typically taken as a quiescent, stratified fluid. Boundary conditions are for the most part conventional. The solid walls are impermeable, no-slip surfaces along which both ψ and its normal derivative are zero. Along the axis the conditions $\psi = \omega = \partial\theta/\partial r = 0$ are employed. All boundaries are at temperature $\theta = 0$, except for the heat source at $r < \frac{1}{2}$ where $\theta = 1$. At the edge of the heat source, $r = \frac{1}{2}$, the temperature is taken as $\theta = \frac{1}{2}$.

The next two sections describe the numerical method and the experimental apparatus used to obtain solutions of the previously stated problem.

3. Numerical method

Equations (2)–(5) with appropriate boundary conditions are solved with a time-marching, finite-difference technique. Forward time and central space differences are used except for the convection terms in (4) and (5) for which conserving, upwind differencing is employed. Details of the technique are similar to Torrance & Rockett (1969) and only the essential differences will be noted.

The calculation proceeds by explicitly advancing θ and ω with difference forms of (4) and (5). A difference form of equation (3) is then solved for the new ψ field by an efficient, cyclic reduction algorithm (Sweet 1974). Such a direct, non-iterative solution for ψ was found to be essential for the present problem, as discussed in the results section. Velocities and boundary vorticity are obtained from the new ψ field by using kinematically consistent difference approximations (Parmentier & Torrance 1975). Such approximations are fully mass conserving in curvilinear co-ordinates. All fields are known and current and the calculation can proceed with a further time advancement. Stability of the scheme follows by restricting the time step; no restrictions are imposed on the spatial mesh.

The finite difference approximations conserve mass, vorticity, and thermal energy within the grid system. As a consequence, the net heat transport from boundary mesh points into the enclosure just balances the net increase of thermal energy within the mesh system. Local and global heat transfer rates at the boundaries are obtained by writing heat balances on half- or quarter-volume elements adjacent to the boundary. Interior fluxes are those used in the finite difference solution. Fluxes parallel to the boundary are included.

The numerical results presented here employed a 41×31 mesh in the x, r directions, with a total of 1271 mesh points. Calculations were first made on a 21×21 mesh over a larger and denser parameter set to delineate trends. Subsets were selected for refinement and presentation here. Comparisons of global quantities such as heat flow and rate of fluid circulation, and local quantities such as the maximum velocity, suggest that results for the fine mesh are correct to 5–10 % when $Gr \leqslant 10^5$, and to 15 % when $Gr = 10^6$. These numbers apply for $Pr = 0{\cdot}7$ and $0{\cdot}05 \leqslant \Gamma \leqslant \infty$. Streamline and isotherm patterns for the two meshes are, for practical purposes, identical. A single time step for the fine mesh calculations required 0·1 seconds on a CDC 7600 electronic computer, and 0·5 seconds on a CDC 6600. Steady states were achieved after $1-2K$ time steps when $Gr \leqslant 10^5$, and after $3K$ time steps when $Gr = 10^6$. Owing to the presence of slowly decaying internal gravity waves, both heat flux and circulation were monitored as sensitive indicators of the approach to steady state. When the heat balance closed and circulation was constant (both to $O(10^{-7})$ or better) steady state was achieved.

4. Experimental apparatus

A light-beam/smoke-particle method was employed to visualize and photograph flow patterns in a stably stratified enclosure. The experiment provides a graphical comparison with calculated streamline patterns over a limited range of parameters, and serves to indicate the limits of an axisymmetric analysis. The apparatus is similar to one described earlier by Torrance, Orloff & Rockett (1969). Only pertinent details are noted here.

Dimensions of the cylindrical enclosure used for the experiment are as follows: 12·4 cm radius, 12·7 cm height, 6·4 mm pyrex walls and 2·4 mm thick copper ceiling. The enclosure base is a 12·7 mm thick aluminium plate of 61 cm × 61 cm horizontal dimensions. To ensure good thermal contact, a sealing grease is used where the pyrex contacts ceiling and floor.

A disk heat source of 38·1 mm diameter, 6·4 mm thick copper is embedded flush with the surface of the aluminium base. A 3·2 mm air gap separates the heat source from the base plate, and yields an effective diameter for the heat source of about 41·3 mm.

The aluminium base plate is cooled from below by room temperature air. The ceiling and disk heat source are heated electrically with nichrome resistance wires. The wires are spaced to yield essentially uniform surface temperatures. The vertical wall is heated with nine independently controlled resistance wires to obtain an internal surface temperature which varies linearly from floor to ceiling. Temperatures on the interior surface of the enclosure are monitored with twelve shielded, 0·13 mm diameter, copper-constantan thermocouples. An insulating hood is placed over the test chamber and camera to eliminate external disturbances.

The light beam is an intense sheet of light provided by three 500 W tungsten iodide lamps, a cylindrical condensing lens, and vertical collimating slits. The beam passes through the centre of the chamber. Smoke from an oil-soaked cigar is added with negligible momentum through a small hole in the centre of the heated disk. Scattered light is recorded on a 10·2 cm × 12·7 cm plate camera with ASA 3000 film. Time exposures of approximately one second were used.

5. Results

Flow fields and temperature fields for ranges of Grashof number (*Gr*), stratification ratio (Γ), and Prandtl number (*Pr*) are examined in the following three sections. For both the experimental and numerical studies the enclosure geometry was held fixed with height A and radius B equal to 3. The corresponding aspect ratio (height/radius $= A/B$) is unity and the relative heat source size (heat source radius/enclosure radius) is $\frac{1}{6}$. Heat transfer rates, velocity profiles, temperature profiles, and the scaling of results are considered in later sections.

5.1. *Effect of Grashof number* (*Gr*)

The variation of steady-state streamline and isotherm fields with *Gr* is illustrated in figure 2. The organization of this figure is similar to others appearing later in the paper. Isotherm fields are shown to the left of the enclosure centreline; streamline fields are shown to the right. The heat source on the floor is indicated by a heavy line. Contour locations were determined by linear interpolation, and positive and negative contours are shown by solid and dashed lines, respectively. As noted earlier, the solid walls and centre-line have value $\psi = 0$. The solid walls also correspond to $\theta = 0$, except for the heated disk in the floor which is at $\theta = 1$. Stream function maxima are indicated by crosses; minima by filled circles. Positive and negative ψ values respectively correspond to clockwise and counter-clockwise circulation. Streamlines are spaced at intervals of 0·1 or 0·2 of the principal maxima and minima in the field. Isotherm temperatures, θ, are indicated.

In figure 2, individual graphs from (*a*) to (*f*) pertain to a sequence of Grashof numbers from 10^2 to 10^7. Other parameters are held constant at $\Gamma = 0{\cdot}3$ and $Pr = 0{\cdot}7$. Therefore, figure 2 may be viewed as illustrating the effect of varying ΔT_H in equations (6), with the ratio $\Delta T_H/\Delta T_V$ held fixed. With $\Gamma = \Delta T_H/\Delta T_V = 0{\cdot}3$, a fluid parcel at the temperature of the heat source will be in buoyant equilibrium at an altitude of 30 % of the enclosure height. At high values of *Gr* in figure 2, it is apparent that circulation in the primary vortex (the one nearest the floor) tends to be confined by the ambient stratification to an elevation which is somewhat less than the aforementioned equilibrium height.

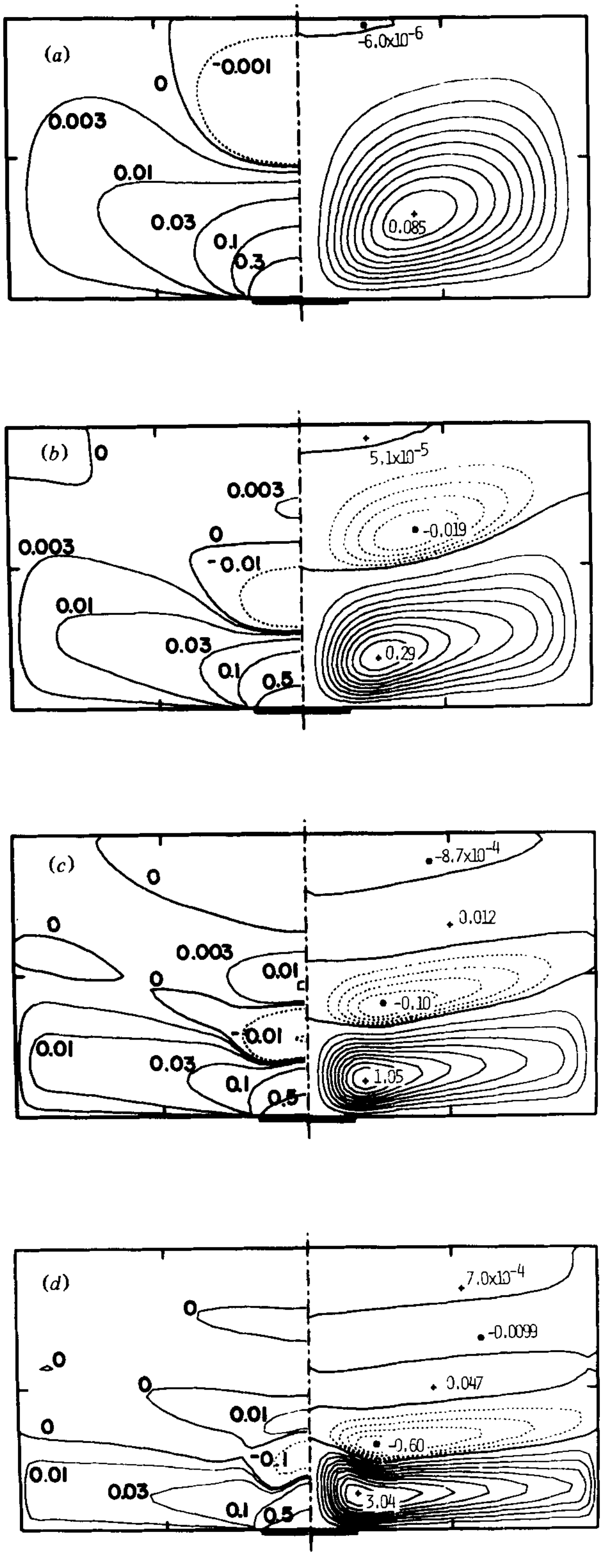

FIGURE 2(*a*)-(*d*). For legend see next page.

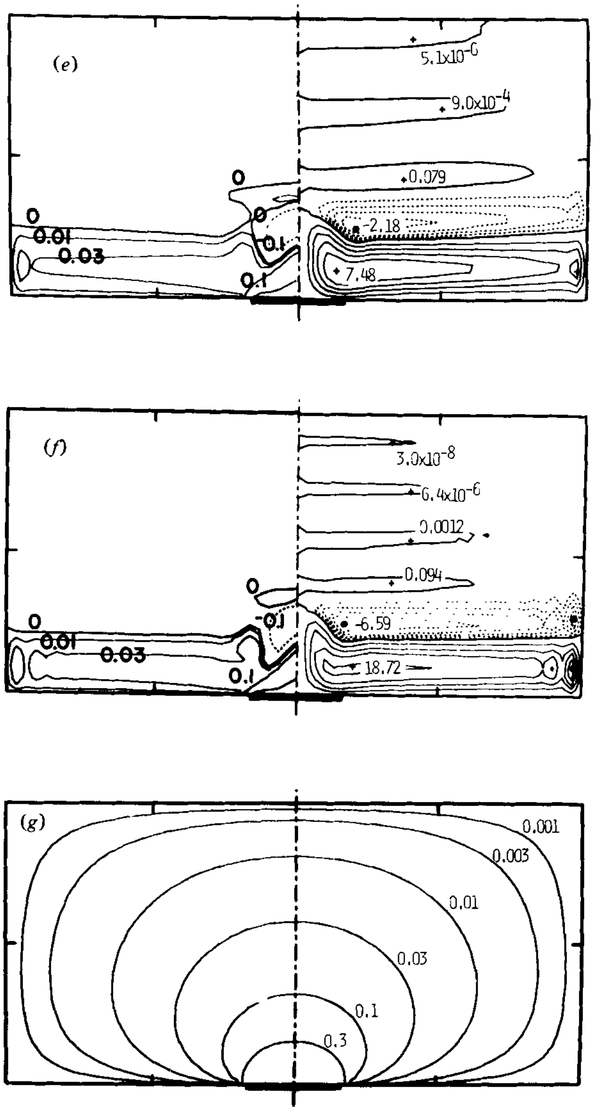

FIGURE 2. Steady-state streamlines (right half) and isotherms (left half) for various Grashof numbers (Gr). Maxima and minima of stream function (ψ), and isotherm temperatures (θ), are indicated. $\Gamma = 0{\cdot}3$ and $Pr = 0{\cdot}7$. (*a*) $Gr = 10^2$; (*b*) $Gr = 10^3$; (*c*) $Gr = 10^4$; (*d*) $Gr = 10^5$; (*e*) $Gr = 10^6$; (*f*) $Gr = 10^7$; (*g*) conduction.

Figure 2 (*a*) illustrates a flow at $Gr = 10^2$ in which both viscous and heat-conduction effects are important. A rolling vortex is centred just below the mid-height and the mid-radius of the enclosure, with a weak, secondary vortex near the ceiling. The influence of fluid motion on the isotherm field is apparent by comparison with the static, no-motion, conduction field shown in figure 2 (*g*). Since θ is defined relative to the ambient temperature gradient, regions of positive θ correspond to temperatures which are locally warmer than ambient. Such regions may form either by heat conduction from the disk heat source or by convection of fluid from regions of higher ambient temperature. Regions of negative θ, on the other hand, are formed only by convection of fluid from regions of low ambient temperature to regions of higher ambient temperature. For this reason negative θ-values are observed at the top of figure 2(*a*). In the absence of ambient stratification (i.e. $\Gamma = \infty$), the flow at $Gr = 10^2$ (not shown) yields a single vortex centred at mid-height and mid-radius. The corresponding temperature field is indistinguishable from the static conduction field.

As Gr is increased in figures 2(*b*) through 2(*f*), the vortex centre moves down and toward the axis. The maximum value of stream function increases, indicating that more fluid circulation exists in the increasingly confined primary vortex. The development of a strong, axial plume is also apparent for $Gr > 10^4$ as streamlines concentrate near the axis. Flow along the axis is first accelerated vertically, and then decelerated, as streamlines converge and diverge. The vertically accelerated plume tends to overshoot its equilibrium height (as revealed by negative isotherms), resulting in a hump in the $\psi = 0$ streamline above the heat source. Away from the axis, the equilibrium height of the $\psi = 0$ streamline is 20 %. Since the plume is not isothermal, this value is less than that expected for a fluid parcel which remains at the temperature of the heat source.

The number of layered convection cells increases in figure 2 from two at $Gr = 10^2$ to ten at $Gr = 10^7$. Cells with negative circulation exist in the open regions between the closed positive cells in the upper halves of graphs (*e*) and (*f*). In all cases, the most vigorous fluid motion is concentrated in the lowest cell. In the higher cells, fluid motion is primarily horizontal and the intensity decreases rapidly with height. The isotherm fields on the left display the effect of plume development near the heated disk. For $Gr > 10^4$, isotherms above the primary vortex indicate a region which is thermally stratified at essentially the ambient rate.

The theoretical streamlines shown in figure 2 may be compared with steady-state, experimental streak photographs for similar values of $\Gamma = 0{\cdot}3$ and $Pr = 0{\cdot}7$ (air). The experimentally observed flows are shown in figures 3(*a*) to 3(*c*) (plate 1) which respectively correspond to $Gr = 4{\cdot}7 \times 10^4$, $1{\cdot}8 \times 10^5$, and $4{\cdot}1 \times 10^5$. Fluid properties appearing in the Grashof number are evaluated at the temperature of the base, T_0, since the principal fluid motion is concentrated near the floor. The development of a plume with increasing Gr is apparent, as is the emergence of an overshoot in the dividing streamline above the heated disk. The existence of a set of vertically layered convection cells above the primary vortex is suggested. Such cells were often seen visually, but they appeared in relatively few of the photographs.

To facilitate comparison of theory and experiment, a side-by-side comparison of streamlines is shown in figure 4 for $\Gamma = 0{\cdot}3$. On the right is a calculated flow at $Gr = 10^5$ (taken from figure 2*d*). On the left are streamlines for the closest experimental conditions, $Gr = 9{\cdot}4 \times 10^4$. The experimental streamlines were sketched using a pantograph from a streak photograph which was too faint for reproduction here. Theory and experiment are seen to be in good agreement in terms of cell geometry and location of the vortex centres. Quantitative comparisons of velocities were not attempted.

The steady-state, theoretical flows shown in figure 2 were obtained by carrying the numerical solution of the initial-value problem forward in time until steady conditions prevailed. The achievement of a true steady state introduced some difficulties, however, as a result of weakly damped internal gravity waves. In figure 5 the maximum value of stream function, $\psi_{\max}$, is shown for a representative flow as a function of time. Parameters correspond to the flow shown in figure 2(*e*): $Gr = 10^6$, $\Gamma = 0{\cdot}3$, and $Pr = 0{\cdot}7$.

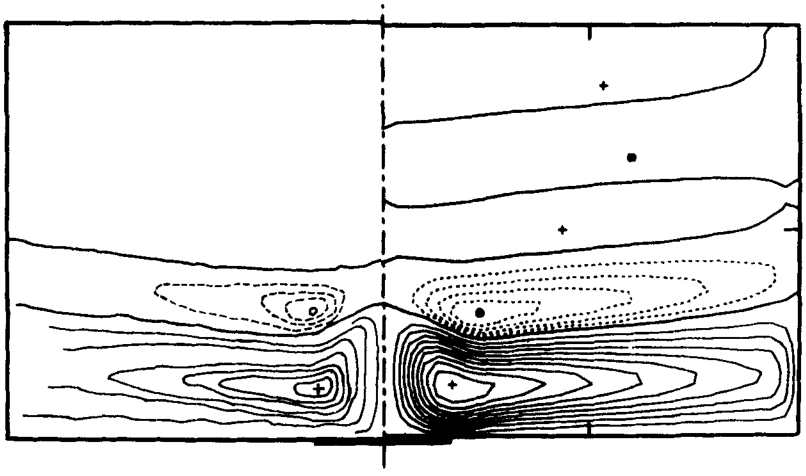

FIGURE 4. Comparison of streamlines at $\Gamma = 0{\cdot}3$, $Pr = 0{\cdot}7$. Right half: calculated at $Gr = 10^5$. Left half: experiment at $Gr = 9{\cdot}4 \times 10^4$.

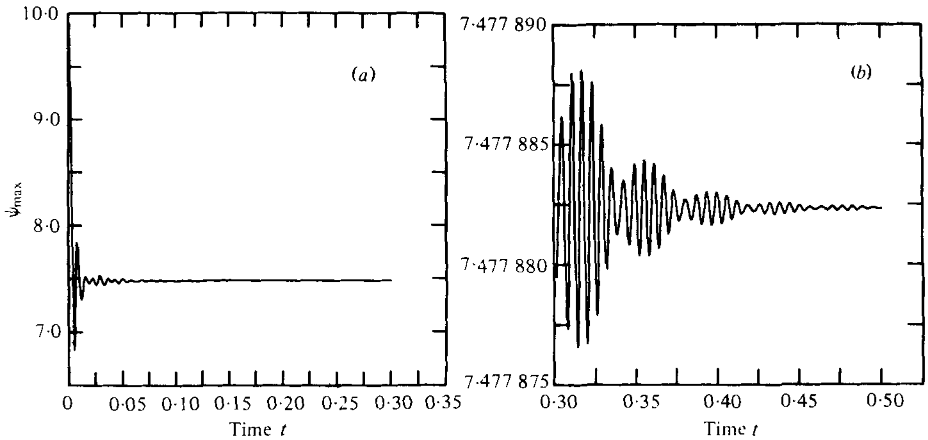

FIGURE 5. Transient evolution of stream function maximum ($\psi_{\max}$) illustrating internal gravity waves and enclosure resonance. $Gr = 10^6$, $\Gamma = 0{\cdot}3$, $Pr = 0{\cdot}7$.

Starting from initial data, $\psi_{\max}$ evolves in an oscillatory fashion in figure 5(*a*) to an apparent steady state at $t = 0{\cdot}30$. Upon restarting the calculation with a greatly expanded ordinate for $\psi_{\max}$ in figure 5(*b*), the periodic nature of the transient becomes apparent. A high-frequency oscillation occurs at very nearly the Brunt–Väisälä frequency, which is the high-frequency cut-off for horizontally propagating gravity waves in a stably stratified fluid. In terms of present notation, the Brunt–Väisälä period corresponding to figure 5 is given (Haltiner 1971, p. 24) by

$$2\pi(A\Gamma/Gr\,Pr^2)^{\frac{1}{2}} = 0{\cdot}00873.$$

The low-frequency overtone in figure 5(*b*) is due to a resonance within the enclosure.

Detailed study of the transients reveals that the internal gravity waves appear as oscillations from side-to-side of the upper cells in figure 2(*e*). As time proceeds, the lowest cell achieves a steady state first, then the cell above it, and so on. Oscillations at the level of 10^{-7}, as shown near $t = 0{\cdot}45$ in figure 5(*b*), are associated with the uppermost eddy. The upper cells look substantially different at $t = 0{\cdot}45$ than at $t = 0{\cdot}30$, after viscosity acts to damp the internal gravity waves. True steady conditions are obtained only after all cells have stabilized. For comparison, a non-dimensional time of $t = 0{\cdot}5$ corresponds to 24 seconds in the laboratory experiments, with an associated Brunt–Vaisala period (at $Gr = 10^6$, $\Gamma = 0{\cdot}3$) of 0·42 seconds.

It is worth noting that early efforts to calculate the flows in figure 2 were unsuccessful for $Gr \gtrsim 10^4$. At that time, a difference approximation to the Poisson equation (3) was solved for ψ by successive-over-relaxation. For practical reasons, iteration was terminated when ψ converged iteratively to $O(10^{-4})$ to $O(10^{-5})$. This 'noise' generated spurious internal gravity waves which triggered a resonant flip-flop of two large vortices within the enclosure. The problem and the non-physical solutions were eliminated by solving the Poisson difference equations to $O(10^{-11})$ by cyclic reduction (Sweet 1974).

The effect of increasing Gr was also explored for a larger value of the stratification ratio Γ, $\Gamma = \Delta T_H/\Delta T_V = 0{\cdot}5$. Trends of the calculated flows are generally similar to those shown for $\Gamma = 0{\cdot}3$ in figure 2 except that the buoyant equilibrium height of the primary cell is higher, indicating the reduced influence of vertical stratification. The laboratory flows are qualitatively similar to the calculated flows up to $Gr = 1{\cdot}7 \times 10^5$. At that point, the laboratory experiments reveal the onset of an azimuthal instability. The top of the rising plume initiates a non-axisymmetric mode and is observed to rotate about the centreline of the enclosure. (This mode also appears in figure 7(*c*), plate 2, which will be discussed later.) The rate of rotation increases with increasing Gr. The numerical calculations assume axisymmetry and reveal no such oscillations. The laboratory experiments therefore indicate the limits of an axisymmetric analysis for $\Gamma = 0{\cdot}5$ to be about $Gr = 1{\cdot}7 \times 10^5$. For $\Gamma = 0{\cdot}3$, no instabilities were observed over the experimentally achievable range of Gr (essentially that shown in figure 3).

5.2. *Effect of stratification ratio* (Γ)

Figure 6 illustrates the effect of varying Γ with the Grashof number fixed at 10^5 and with $Pr = 0{\cdot}7$. In figure 6, increasing Γ while holding Gr fixed may be interpreted as reducing the stratification temperature difference ΔT_V while holding the natural convection driving force ΔT_H fixed. The case $\Gamma = 0{\cdot}05$ in figure 6(*a*) corresponds to a strong ambient stratification. The buoyant equilibrium height of the primary cell above the heated disk is 0·08 of the chamber weight. Increasing Γ intensifies the plume and the amount of fluid circulation, and increases the buoyant equilibrium height. For $\Gamma = 4$ and 10, the plume impacts the ceiling and a ceiling jet forms. In the absence of stratification, $\Gamma = \infty$, a simple, natural convection flow driven by the heated disk is obtained. This flow is in accord with earlier results obtained for a somewhat smaller heat source (Torrance & Rockett 1969). In figure 6, it is significant to observe that a relatively weak stratification, $\Gamma = 10$, has an influence on the ceiling jet. This point will be given additional attention in a later section.

The flows shown in figure 6 may be compared, at least qualitatively, with experimental flows at $Gr = 1{\cdot}3 \times 10^5$ in figures 7(*a*)–(*c*) (plate 2) which correspond to $\Gamma = 0{\cdot}2$, 0·4, and 0·83. The experimental flows at the lower values of Γ are similar to those shown earlier in figure 3 (plate 1) and the sequence as a whole illustrates the emerging and intensifying axial plume. A relatively weak azimuthal instability is apparent at

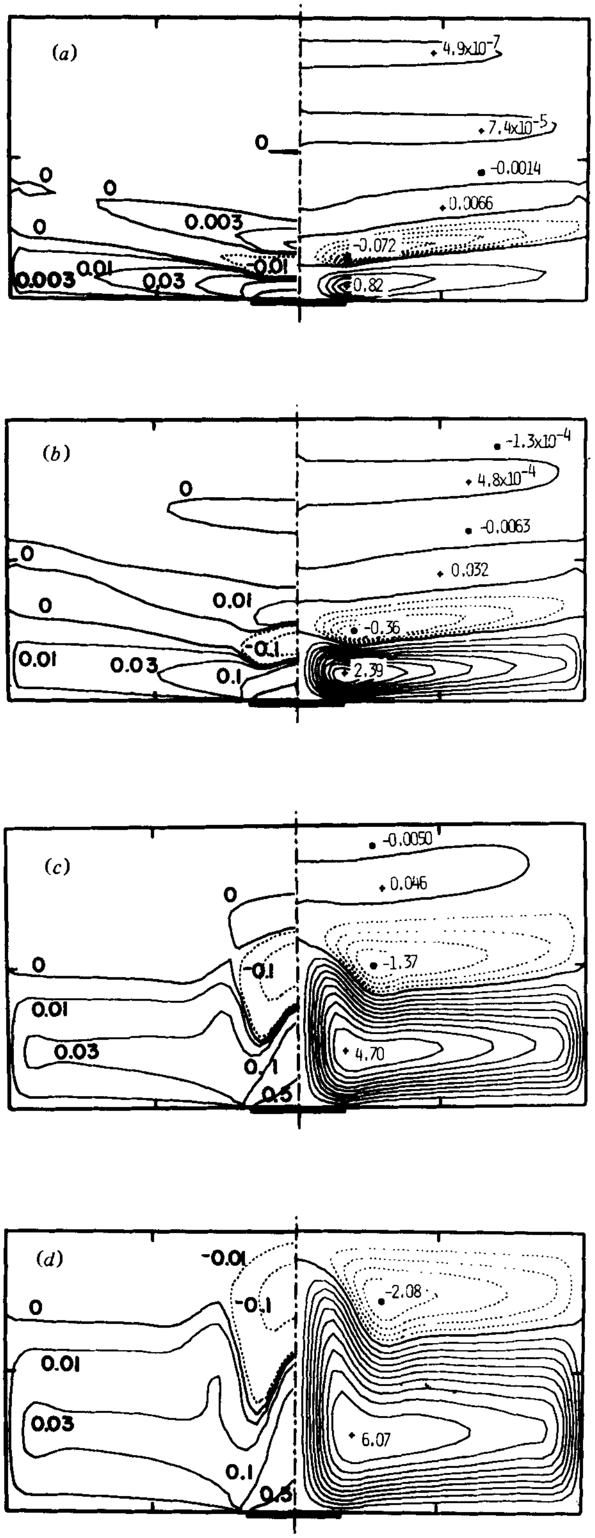

FIGURES 6(*a*)–(*d*). For legend see next page.

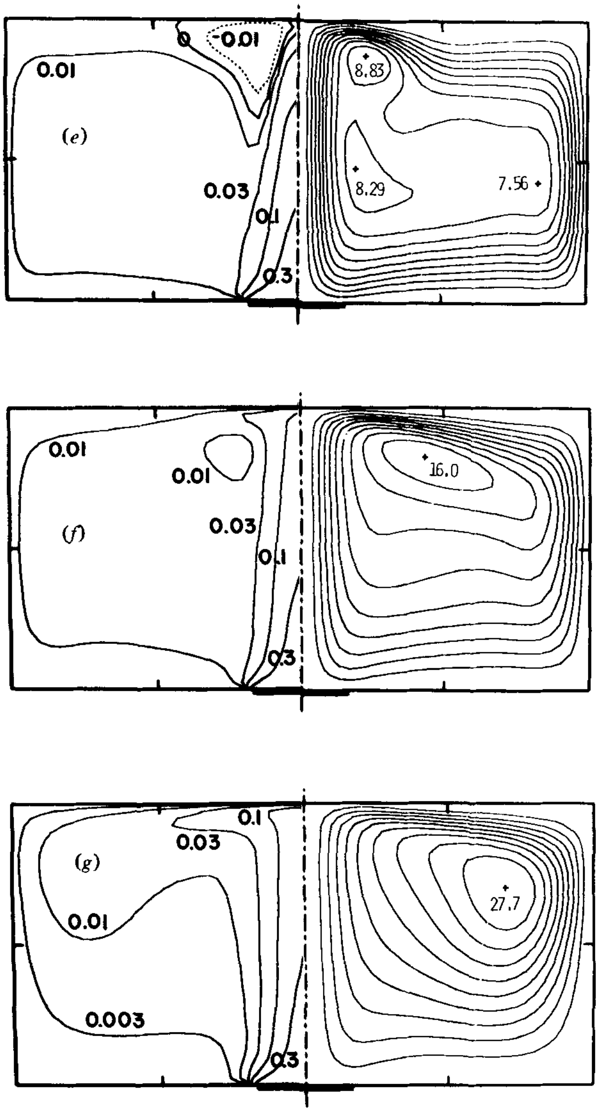

FIGURE 6. Steady-state streamlines and isotherms at $Gr = 10^5$ and $Pr = 0{\cdot}7$ for various stratification ratios (Γ). $\Gamma = 0{\cdot}05$ corresponds to strong stratification and $\Gamma = \infty$ to no stratification. Maxima and minima of streamfunction (ψ), and isotherm temperatures (θ), are indicated. (a) $\Gamma = 0{\cdot}05$; (b) $\Gamma = 0{\cdot}2$; (c) $\Gamma = 0{\cdot}8$; (d) $\Gamma = 1{\cdot}6$; (e) $\Gamma = 4{\cdot}0$; (f) $\Gamma = 10{\cdot}0$; (g) $\Gamma = \infty$.

$\Gamma = 0{\cdot}83$, and is visually observed to disappear for $\Gamma \gtrsim 2$. The experiments thus suggest that the axisymmetric flows in figure 6 may be subject to an azimuthal instability for a range of Γ-values in the interval between 0·5 and 2.

The multicellular flow shown in figure 6(a) was found to persist, albeit with more cells, in test calculations with stronger stratification (i.e. $\Gamma < 0{\cdot}05$). In all cases, the primary vortex extended to the outer wall of the enclosure. The dividing streamline did not reattach to the floor and thus initiate a closed recirculation zone around the heated disk.

To ascertain whether the multicell structure of figure 6(a) would persist at lower

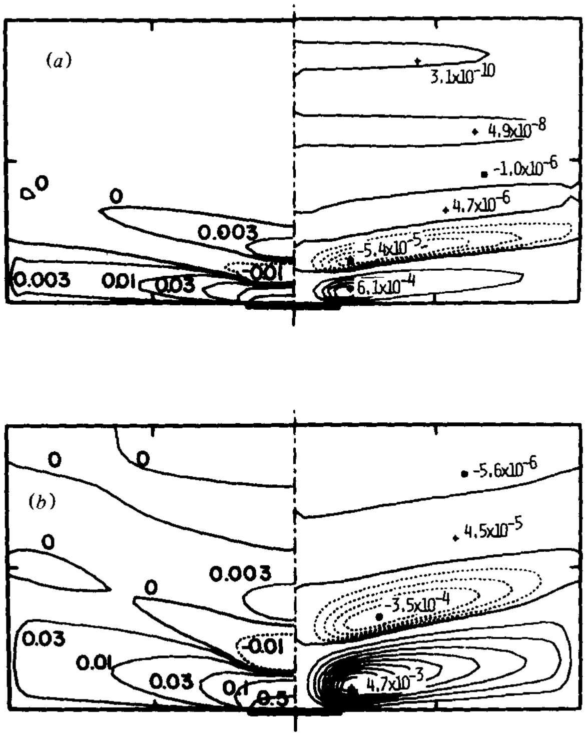

FIGURE 8. Streamlines and isotherms at a low value of *Gr*, $Gr = 10^2$. Results shown for two values of stratification ratio and $Pr = 0{\cdot}7$. (*a*) $\Gamma = 0{\cdot}00005$; (*b*) $\Gamma = 0{\cdot}0016$.

values of Grashof number, the flows illustrated in figure 8 were obtained. For this figure, $Gr = 10^2$ and $Pr = 0{\cdot}7$. The multicellular structure persists for the two stratification ratios shown. A useful scaling may be deduced. For viscous-dominated flows, the right side of the momentum equation (4) suggests that velocities scale as $u \sim Gr\,Pr$. For the case of strong stratification, we expect the term $u/A\Gamma$ to dominate in the energy equation (5). Thus, for flows which are both viscous and strongly stratified, we expect the governing parametric group to be $Gr\,Pr/A\Gamma$. The flows in figures 6 (*a*) and 8 (*a*) are in this category; parameters were selected so that for both flows

$$Gr\,Pr/A\Gamma = 4{\cdot}67 \times 10^5.$$

The similarity between the flows is quite striking. Corresponding ψ and θ contours are virtually indistinguishable when overlaid. The ψ values differ in magnitude, of course, since u (and ψ) scale with $Gr\,Pr$ in a viscous regime. ψ-Values in figure 6 (*a*) are roughly 10^3 times those in figure 8 (*a*). The scaling breaks down as inertial effects become important, as evidenced by the flows in figures 6 (*d*) and 8 (*b*) which both correspond to $Gr\,Pr/A\Gamma = 1{\cdot}46 \times 10^4$.

5.3. *Effect of Prandtl number* (*Pr*)

In the preceding discussions the Prandtl number was held fixed at $Pr = 0{\cdot}7$. We will now examine the influence of Prandtl number on the flows. Results are shown in figure 9 for $Pr = 0{\cdot}01$ and $Gr = 10^5$. A Prandtl number reduction may be achieved by increasing the thermal diffusivity κ when all other parameters are held fixed. In turn,

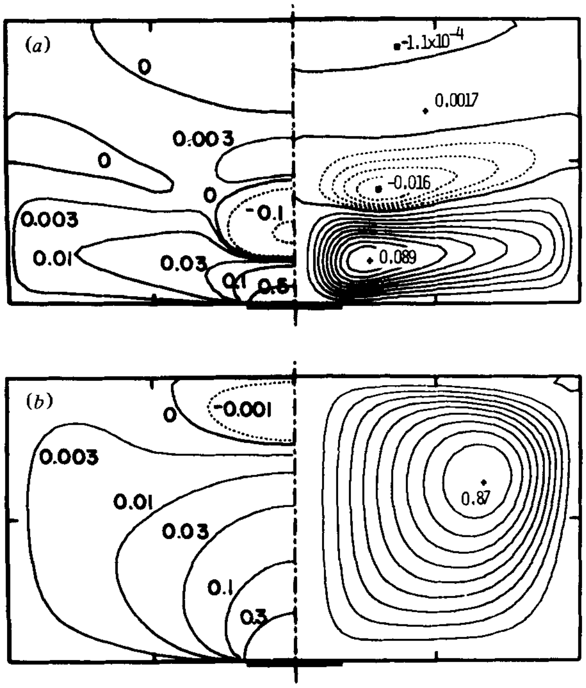

FIGURE 9. Streamlines and isotherms for a low Prandtl number fluid, $Pr = 0{\cdot}01$. Results shown for two values of stratification ratio and $Gr = 10^5$. (a) $\Gamma = 0{\cdot}05$; (b) $\Gamma = 5{\cdot}0$.

an increase in κ could simulate, at least qualitatively, the contribution of radiative transfer and its influence on the observed cellular flows.

The flows in figure 9 thus correspond to a higher value of thermal diffusivity than corresponding flows in figure 6. As a consequence, the thermal plume in figure 9(b) is virtually eliminated as compared to figure 6(e), and a broader velocity plume results. Similar effects are observed for $\Gamma = 0{\cdot}05$ in figures 9(a) and 6(a). It is apparent that an increase in κ influences the flow structure, but a multicell pattern still persists.

The flows in figure 9 provide a further test of the viscous-regime, strong-stratification scaling discussed in the preceding section. Again, using $Gr\,Pr/A\Gamma$ as the scaling measure, flows with similar values of this parameter may be compared. The flows in figures 9(a) and 2(c) form such a pair and correspond to $Gr\,Pr/A\Gamma \approx 7000$. The streamline fields are quite similar, and the temperature fields generally similar. Again, ψ scales roughly with $Gr\,Pr$. The flows in figures 9(b) and 2(a) also form a pair and correspond to $Gr\,Pr/A\Gamma \approx 70$. Only the gross features of the ψ and θ fields are comparable, however, presumably due to the relatively greater influence of inertia (and thus convection) in figure 9(b) as compared to figure 2(a).

5.4. *Velocity and temperature profiles, heat transfer rates, and trends with Gr and* Γ

Velocity and temperature profiles at the centre-line and the mid-radius of the enclosure are illustrated in figure 10. The upper row corresponds to the sequence of flows at $\Gamma = 0{\cdot}3$ shown in figure 2, while the lower row corresponds to the sequence at $Gr = 10^5$

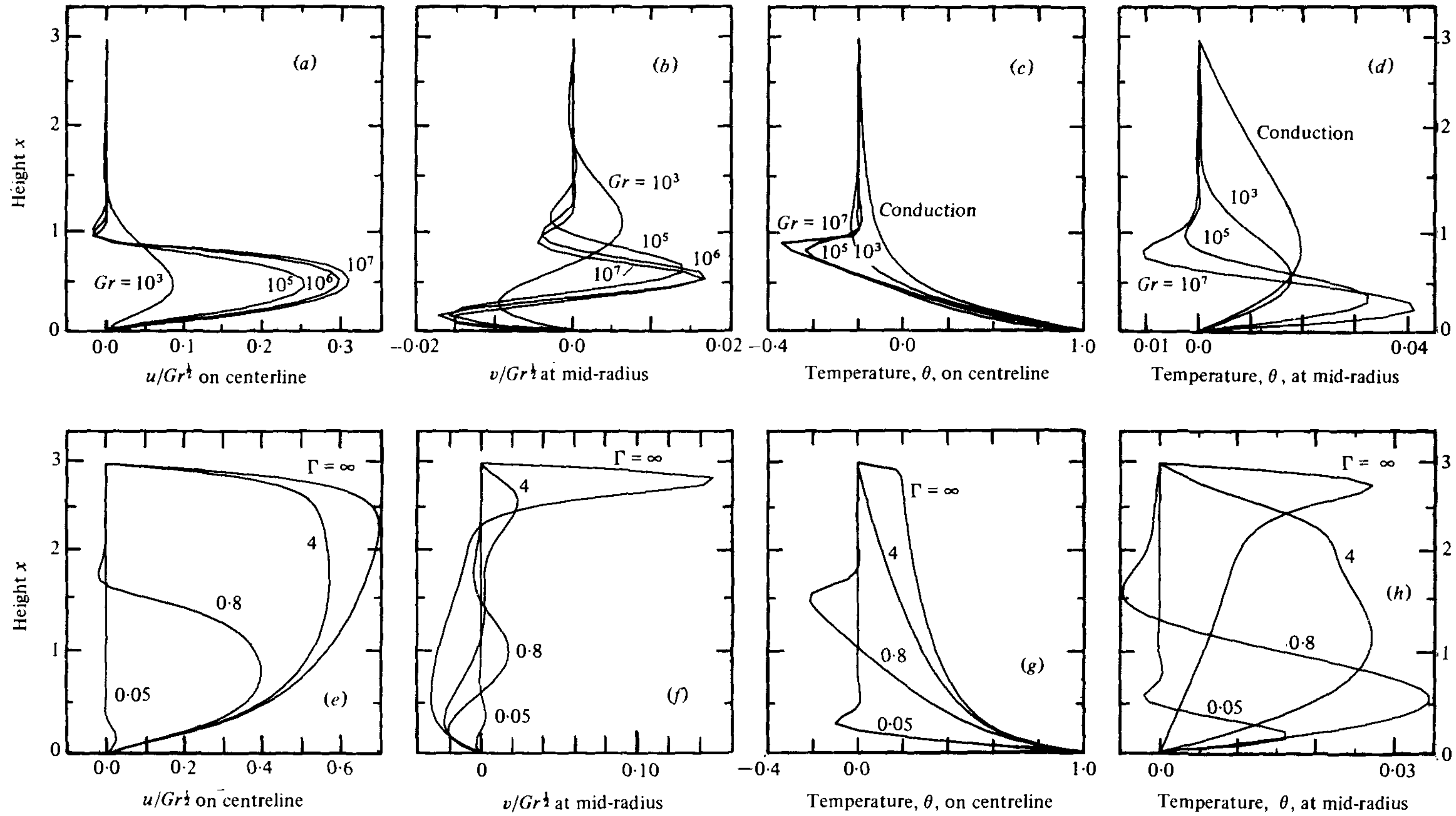

FIGURE 10. Vertical profiles of vertical velocity (u), horizontal velocity (v), and temperature (θ). (a)–(d) Profiles for various Grashof numbers (Gr) with $\Gamma = 0{\cdot}3$ and $Pr = 0{\cdot}7$. (e)–(h) Profiles for various stratification ratios (Γ) with $Gr = 10^5$ and $Pr = 0{\cdot}7$. (a)–(d) correspond to figure 2; (e)–(h) correspond to figure 6.

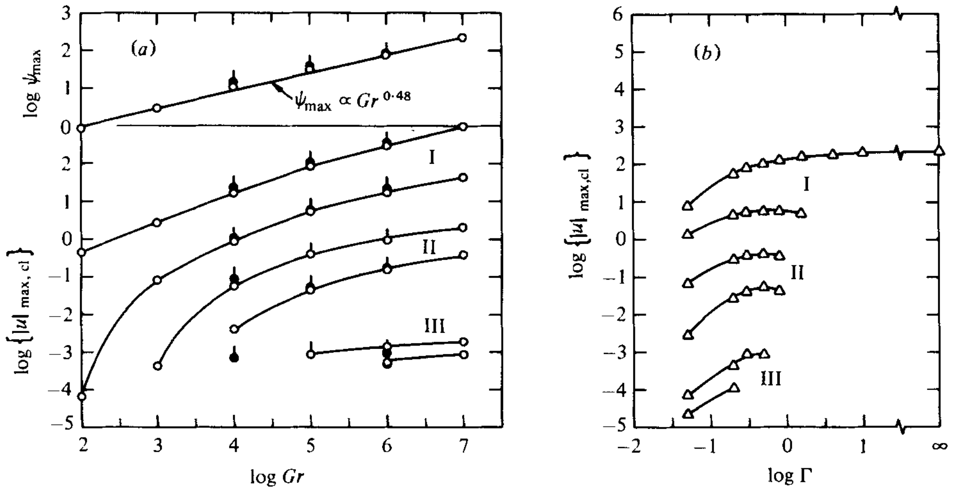

FIGURE 11. Maximum stream function, ψ_{max}, and absolute value of vertical velocity maxima on the centre-line, $|u|_{max,cl}$. (*a*) *Versus Gr* for $\Gamma = 0{\cdot}3$ and $Pr = 0{\cdot}7$; (*b*) *versus* Γ for $Gr = 10^5$ and $Pr = 0{\cdot}7$. (*a*) and (*b*) correspond to the flow sequences in figures 2 and 6, respectively.

shown in figure 6. Thus, the upper and lower rows respectively illustrate the effect of varying *Gr* or Γ, with other parameters held fixed. All velocity profiles are normalized by the parameter $\sqrt{Gr}$. This scaling follows from the basic equations (2)–(4). For the case when inertia and buoyancy forces dominate, velocities should scale as

$$u \sim (Gr\,Pr^2)^{\frac{1}{2}};$$

and when viscous and buoyancy effects dominate, the implied scaling is $u \sim Gr\,Pr$.

The vertical velocity along the centre-line, figure 10 (*a*), and the horizontal velocity at the mid-radius, figure 10 (*b*), confirm the validity of the $\sqrt{Gr}$ scaling at large *Gr*. For $Gr > 10^5$, the velocity profiles are essentially identical. It is apparent that the regions of large velocities are confined to the primary and secondary cells near the floor. The centre-line and mid-radius temperature profiles in graphs (*c*) and (*d*) also reveal a similarity in shape for $Gr > 10^5$. Above the primary and secondary cells the ambient temperature gradient prevails.

The lower row of graphs reveals a marked dependence of the profiles upon the stratification ratio Γ. As Γ increases from strong stratification ($\Gamma = 0{\cdot}05$) to no stratification ($\Gamma = \infty$), a systematic variation from a weak, confined primary vortex to a freely circulating convective flow is apparent. Indeed, at $\Gamma = \infty$, a strong axial plume and a distinct ceiling jet exist.

Additional scaling information is provided in figure 11, wherein the ordinates are ψ_{max} or the absolute value of the vertical velocity maxima on the centre-line, $|u|_{max,\,cl}$. The abscissae are *Gr* or Γ. The left and right graphs correspond to flows shown in figures 2 and 6, respectively. In the left graph, open and filled circles denote data at $\Gamma = 0{\cdot}3$ and $\Gamma = 0{\cdot}5$. The data are in close agreement, and the curves are drawn through the open circles. In the right graph, all data correspond to $Gr = 10^5$.

In the upper left graph of figure 11, the volume circulation rate of the primary eddy, ψ_{max}, is well described by $\psi_{max} \sim \sqrt{Gr}$. This is characteristic of an inertially dominated, buoyant flow. Along the centre-line, there are several maxima of $|u|$ corresponding to

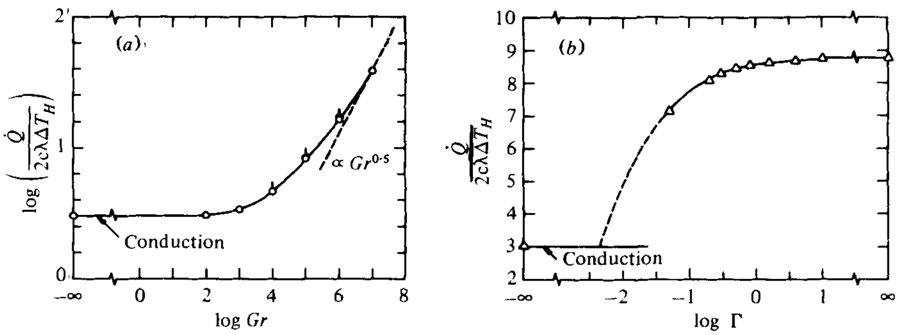

FIGURE 12. Dimensionless rate of total heat transfer into, or out of, the enclosure. (*a*) *Versus* *Gr* for $\Gamma = 0{\cdot}3$ and $Pr = 0{\cdot}7$; (*b*) *versus* Γ for $Gr = 10^5$ and $Pr = 0{\cdot}7$. (*a*) and (*b*) respectively correspond to flows shown in figures 2 and 6.

the individual cells (see figures 2 and 6). These maxima generally represent the highest velocities in the cells. In both left and right graphs, the uppermost curves for $|u|$ represent the primary cell, driven directly by the heated disk in the floor. The next lower curves denote the second cell, the third cell, and so on, when higher cells exist. The data for all cells suggest a pairwise grouping. Pair I consists of the first and second cells; pair II the third and fourth; and so on. Clearly, all cells above the primary cell are driven by viscous shear and the observed pairing is a result of shear coupling.

Velocities in pair I (left graph, figure 11) generally follow a $u \sim \sqrt{Gr}$ dependence at large *Gr* (inertial regime) and a somewhat higher power dependence at lower *Gr* (viscous regime). Pair III and higher pairs are nearly independent of *Gr*. In the right graph $|u|$ is observed to first increase and to then become essentially constant as Γ is increased. At sufficiently large Γ, the higher cells disappear one by one.

The total rate of heat transfer, $\dot{Q}$, into (or out of) the enclosure is illustrated in figure 12. The organization and data symbols are similar to figure 11. The left graph pertains to $\Gamma = 0{\cdot}3$ (open circles) and $\Gamma = 0{\cdot}5$ (filled circles), whereas the right graph corresponds to $Gr = 10^5$ (triangles). The ordinate is made dimensionless with the heated disk diameter $2c$, fluid thermal conductivity λ, and the horizontal temperature difference ΔT_H.

The left graph in figure 12 shows that the rate of heat transfer increases from the static conduction value as *Gr* is increased. At high *Gr*, the rate of heat transfer is proportional to the rate of vertical convection in the rising plume, i.e. $\dot{Q} \sim u$, and in such a regime u varies as $\sqrt{Gr}$. Thus, at high *Gr* the behaviour $\dot{Q} \sim \sqrt{Gr}$ is expected, and is indicated by the dashed line. The right graph in figure 12 reveals that the total rate of heat transfer, $\dot{Q}$, asymptotically approaches the unstratified ($\Gamma = \infty$) value following an abrupt increase from the conduction value. The abruptness of the transition was confirmed by a denser set of calculations with a coarse grid. The abrupt transition is a thermal phenomenon, associated with the horizontal displacement of isotherms by horizontal convection. Fluid motion was observed to exist for all Γ (as low as 10^{-4} at $Gr = 10^5$).

Not illustrated in figure 12, but deserving of some comment, is the effect of varying Γ at lower *Gr* (the flows at $Gr = 10^2$ in figure 8) and at lower *Pr* ($Pr = 0{\cdot}01$ in figure 9). For both of these cases, the trend of $\dot{Q}$ with Γ differs from that shown in figure 12(*b*).

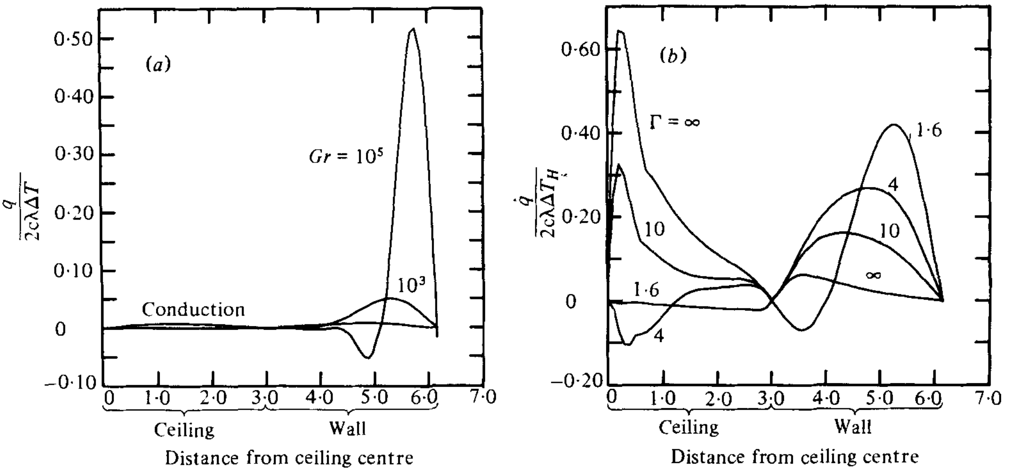

FIGURE 13. Dimensionless rate of local heat transfer along the ceiling and vertical wall of the enclosure. (*a*) Effect of Grashof number for $\Gamma = 0{\cdot}3$ and $Pr = 0{\cdot}7$. (*b*) Effect of stratification ratio for $Gr = 10^5$ and $Pr = 0{\cdot}7$. (*a*) and (*b*) respectively correspond to flows shown in figures 2 and 6.

Following the abrupt transition from the conduction value, $\dot{Q}$ tends to overshoot the asymptotic, $\Gamma = \infty$, values of $\dot{Q}$. Of course, the $\Gamma = \infty$ values of $\dot{Q}$ for both cases are very close to the conduction value (within 4 %). The maxima in $\dot{Q}$ at intermediate values of Γ is a direct result of the low-altitude circulation, which effectively transports heat from the heated disk to the nearby cold floor and walls. For example, for the flow in figure 9 (*a*), the rate of heat transfer is greater than for the flow in figure 9 (*b*).

From the previous discussion, it is apparent that the total rate of heat transfer, $\dot{Q}$, is strongly influenced by the flow patterns and by the local rate of heat transfer, $\dot{q}$, at the boundaries. Indeed, large variations in $\dot{q}$ occur along the ceiling and vertical wall of the enclosure, as illustrated in figure 13. Positive values of $\dot{q}$ correspond to heat removal from the enclosure. The left diagram corresponds to the sequence of flows at $\Gamma = 0{\cdot}3$ shown in figure 2, and the influence of the primary and secondary convection cells on wall heat transfer becomes apparent with increasing Gr. The right diagram corresponds to the sequence of flows at $Gr = 10^5$ in figure 6. Clearly, as Γ is increased from $\Gamma = 1{\cdot}6$ to ∞, the rate of heat transfer diminishes at the vertical wall, and increases along the ceiling.

6. Summary

Plume-like flows are observed to develop in a thermally stratified enclosure as Gr is increased at fixed stratification ratio, Γ (figures 2 and 3), or as Γ is increased at fixed Gr (figures 6 and 7). In the former case, the number of vertically layered convection cells above the plume increases with increasing Gr. In the latter case, the number decreases with increasing Γ. In all cases, the lowest or primary cell extends to the outer wall.

Heat transfer to the walls of the enclosure is altered in both magnitude and spatial distribution as Γ varies. Relatively small amounts of ambient stratification significantly reduce heat transfer to the ceiling (figure 13).

Scaling of velocity and heat transfer with $\sqrt{Gr}$ at large Gr is suggested in figures 10–12. In addition, flow fields are observed to scale with $Gr\,Pr/A\Gamma$ in a viscous, strongly stratified regime.

An azimuthal instability is observed in certain of the laboratory flows (figure 7c), but additional work is required to precisely define the ranges of instability. In the calculations, the presence of weakly damped internal gravity waves made it necessary to solve the finite difference approximation to the stream function equation (3) by a direct, non-iterative method.

The laboratory experiments were supported by the Cornell Energy Project under NSF Grant GI-29903, and were carried out by Mr Eric M. Swensen. The numerical calculations were undertaken by the author during a sabbatical visit in the Advanced Study Program, National Center for Atmospheric Research, Boulder, Colorado. The National Center for Atmospheric Research is supported by the National Science Foundation of the United States.

REFERENCES

CHEN, C. F., BRIGGS, D. G. & WIRTZ, R. A. 1971 Stability of thermal convection in a salinity gradient due to lateral heating. *Int. J. Heat Mass Transfer* **14**, 57.

DELAGE, Y. & TAYLOR, P. A. 1970 Numerical studies of heat island circulations. *Boundary-Layer Mete.* **1**, 201.

HALTINER, G. J. 1971 *Numerical Weather Prediction*. Wiley.

KNIGHT, C. 1976 Numerical studies of natural convection in an enclosure. *Tech. rep.* no. 15, Division of Engineering and Applied Physics, Harvard University, Cambridge, Massachusetts.

PARMENTIER, E. M. & TORRANCE, K. E. 1975 Kinematically consistent velocity fields for hydrodynamic calculations in curvilinear coordinates. *J. Comp. Phys.* **19**, 404.

SWEET, R. A. 1974 A generalized cyclic reduction algorithm. *SIAM J. Numer. Anal.* **11**, 506.

TORRANCE, K. E., ORLOFF, L. & ROCKETT, J. A. 1969 Experiments on natural convection in enclosures with localized heating from below. *J. Fluid Mech.* **36**, 21.

TORRANCE, K. E. & ROCKETT, J. A. 1969 Numerical study of natural convection in an enclosure with localized heating from below – creeping flow to the onset of laminar instability. *J. Fluid Mech.* **36**, 33.

TURNER, J. S. 1973 *Buoyancy Effects in Fluids*. Cambridge University Press.

WALIN, G. 1971 Contained non-homogeneous flow under gravity or how to stratify a fluid in the laboratory. *J. Fluid Mech.* **48**, 647.

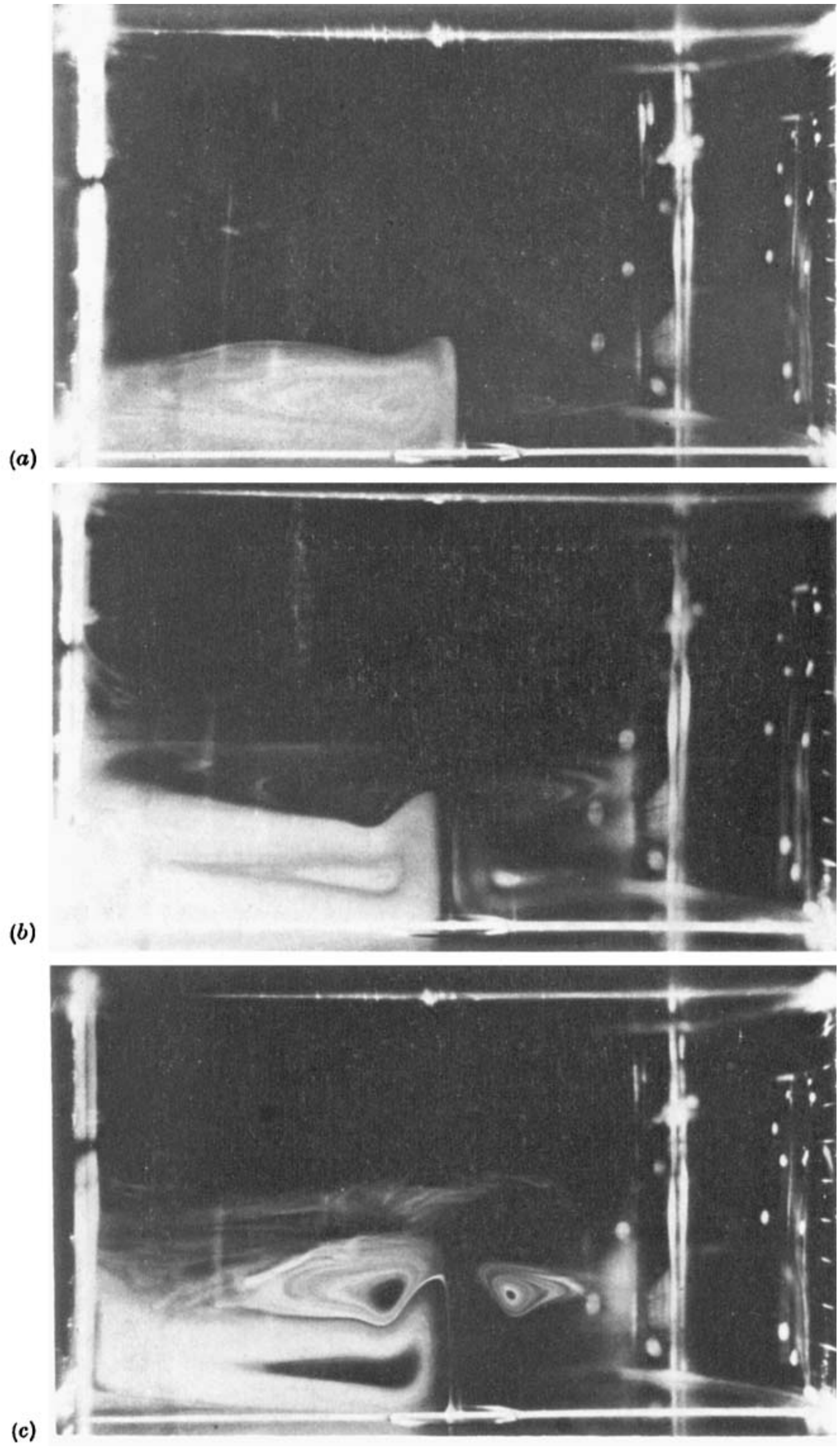

FIGURE 3. Smoke-streak photographs illustrate the effect of varying the Grashof number (Gr) in a cylindrical enclosure. Illumination through the centre of the heated disk on the floor. Stratification ratio $\Gamma = 0{\cdot}3$ and $Pr = 0{\cdot}7$ (air). (*a*) $Gr = 4{\cdot}7 \times 10^4$; (*b*) $Gr = 1{\cdot}8 \times 10^5$; (*c*) $Gr = 4{\cdot}1 \times 10^5$.

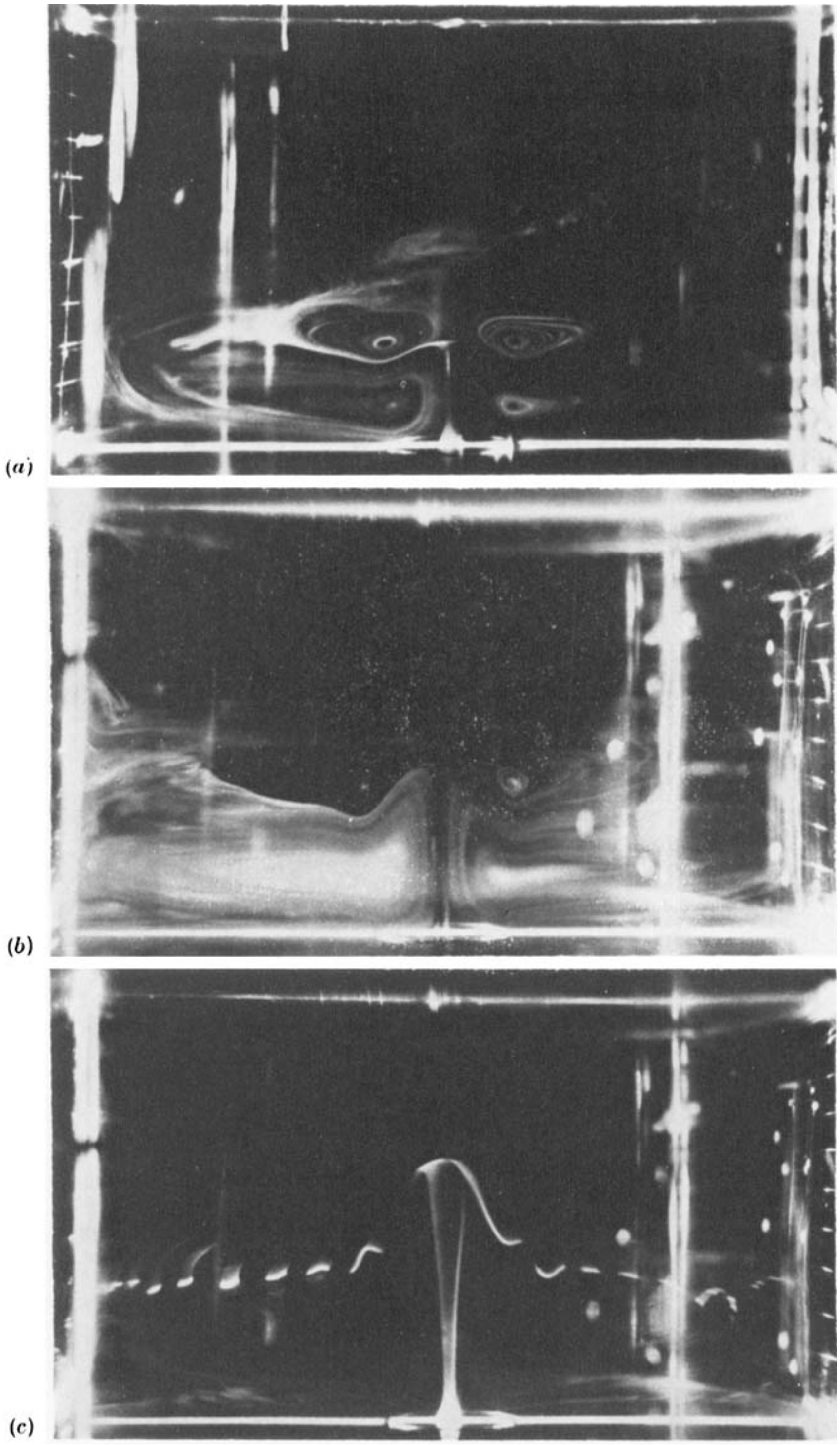

FIGURE 7. Effect of varying the stratification ratio (Γ) in the laboratory experiments for $Gr = 1{\cdot}3 \times 10^5$ and $Pr = 0{\cdot}7$. (*a*) $\Gamma = 0{\cdot}2$; (*b*) $\Gamma = 0{\cdot}4$; (*c*) $\Gamma = 0{\cdot}83$.